PCCP

Intersystem Crossing in Tunneling Regime: $T_1 \rightarrow S_0$ Relaxation in Thiophosgene

Journal:	*Physical Chemistry Chemical Physics*
Manuscript ID	CP-ART-12-2019-006956.R1
Article Type:	Paper
Date Submitted by the Author:	18-Feb-2020
Complete List of Authors:	Lykhin, Aleksandr; University of Nevada, Reno, Department of Chemistry Varganov, Sergey; University of Nevada, Reno, Department of Chemistry

Intersystem Crossing in Tunneling Regime: $T_1 \rightarrow S_0$ Relaxation in Thiophosgene

Aleksandr O. Lykhin[†], Sergey A. Varganov*

Department of Chemistry, University of Nevada, Reno, 1664 N. Virginia Street, Reno, Nevada 89557-0216, United States.

[†]*Present Address: Department of Chemistry, University of Minnesota, Minneapolis, Minnesota 55455-0431, United States.*

*E-mail: svarganov@unr.edu

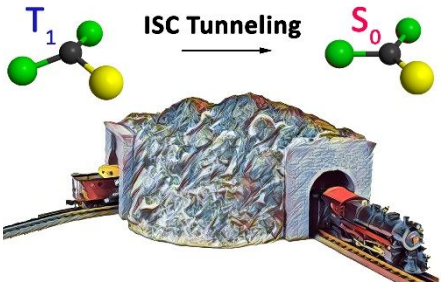

Abstract

The T_1 excited state relaxation in thiophosgene has attracted much attention as a relatively simple model for the intersystem crossing (ISC) transitions in polyatomic molecules. The very short (20-40 ps) T_1 lifetime predicted in several theoretical studies strongly disagrees with the experimental values (~20 ns) indicating that the kinetics of $T_1 \rightarrow S_0$ ISC is not well understood. We use the nonadiabatic transition state theory (NA-TST) with the Zhu-Nakamura transition probability and the multireference perturbation theory (CASPT2) to show that the $T_1 \rightarrow S_0$ ISC occurs in the quantum tunneling regime. We also introduce a new zero-point vibrational energy correction scheme that improves the accuracy of the predicted ISC rate constants at low internal energies. The predicted lifetimes of the T_1 vibrational states are between one and two orders of magnitude larger than the experimental values. This overestimation is attributed to the multidimensional nature of quantum tunneling that facilitates ISC transitions along the non-minimum energy path and is not accounted for in the one-dimensional NA-TST.

1. Introduction

Despite the spin-forbidden nature of intersystem crossings (ISCs), these transitions between electronic states of different spin multiplicities are some of the most ubiquitous and important events in reaction dynamics.[1] Their ubiquity is due to the coupling between electron spin and other types of angular momentum, with the main contribution often arising from the spin-orbit coupling (SOC) that determines the extent to which "spin-forbidden" transitions are actually allowed.[2, 3] Weak SOC, typically observed in molecules with light atoms, results in low probabilities of transition between spin-diabatic states and inefficient ISCs.[4] If a slow ISC is the dominant exited state relaxation mechanism, the molecule can be trapped in an excited state for a long time, which is used to form the long-lived reactive intermediates prone to the intermolecular energy transfer or the spontaneous photon emission.[4] In contrast, strong SOC[5] can lead to the ultrafast ISCs,[6] which can compete with spin-allowed internal conversions giving rise to complex excited state relaxation dynamics.[7-9] Therefore, investigations of ISC kinetics in different regimes are important for understanding the wide range of chemical and physical phenomena, including combustion of organic compounds,[10, 11] light-harvesting in photovoltaics,[12-14] sensitizing in photodynamic therapy,[15-17] depletion of excited states in photoprotection,[18, 19] and binding of small molecules in enzymes.[20, 21]

The accurate prediction of ISC rates is one of the biggest challenges in computational chemistry, which is often addressed with *ab initio* molecular dynamics (NA-AIMD).[22] In direct NA-AIMD, semiclassical trajectories or nuclear wave packets are propagated in time, while electronic energy, energy gradients, and interstate couplings are obtained at each time step by solving the electronic Schrödinger equation. The requirement for the time step to be smaller than

the characteristic time of the fastest molecular vibration makes it challenging to apply NA-AIMD to the slow ISCs happening on a time scale longer than a few ps. In such cases, an alternative approach is to use one of the time-independent statistical theories, such as the microcanonical nonadiabatic transition state theory (NA-TST).[23-27] The keystone of NA-TST is the ergodicity assumption and the statistical treatment of the internal energy distribution among vibrational modes at the critical points on the coupled potential energy surfaces (PESs). A small number of critical points drastically reduces the number of required electronic structure calculations and allows the use of high-level electronic structure methods. In addition, the statistical ISC rates can be corrected for the zero-point energy (ZPE), which is often neglected in NA-AIMD simulations. In NA-TST, the ISC rate constant is proportional to the flux through the minimum energy crossing point (MECP) on the intersection seam between two spin-diabatic PESs of different multiplicities (Figure 1).

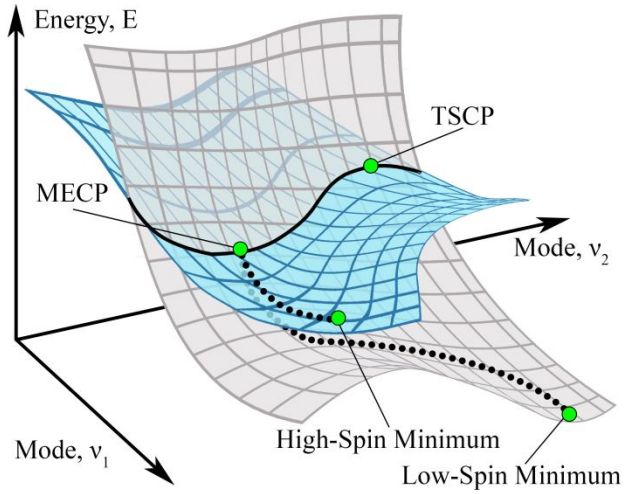

Figure 1. Sketch of the intersecting two-dimensional high- and low-spin PESs. Minimum energy crossing point (MECP) and transition state crossing point (TSCP) correspond to the minimum and maximum (saddle point, if the PES dimensionality > 2) on the crossing seam, respectively. Black dots show the turning points along the ISC minimum energy path.

The ISC rate constant depends on the molecular properties at MECP and the transition probability between the spin states. The MECP can be located using the gradient-based algorithms,[28-30] one of which has been recently extended to large complex systems, such as solvated proteins.[31] Evaluation of transition probability, on the other hand, can be challenging as the available analytical formulas are limited to the ISC regimes with either weak SOC or high internal energy in the reaction coordinate at the crossing seam.[32-34] Recently, there has been growing interest in the Zhu-Nakamura transition probability formulas, which can cover all possible ISC regimes with no energy or coupling strength limitations.[35-40] In this work, we combine the NA-TST and the Zhu-Nakamura transition probability to gain insight into the mechanism of the $T_1 \rightarrow S_0$ ISC in thiophosgene (Cl_2CS).

Spectroscopic properties of thiophosgene make this molecule an excellent model to study the $T_1 \rightarrow S_0$ ISC kinetics from both theoretical[41] and experimental[42-45] perspectives. Despite the formally spin-forbidden nature of $T_1 \leftarrow S_0$ excitation, the "dark" T_1 state can be populated directly using high-intensity laser pulses. Once T_1 state is populated, it decays primarily through the $T_1 \rightarrow S_0$ ISC with a minor contribution from very weak phosphorescence.[46] The time-evolution of T_1 state can be probed by time-delayed laser pulses, which transfer population from T_1 to the "bright" state S_2. Because of the *vibrational deficiency*, S_2 decays exclusively via $S_2 \rightarrow S_0$ fluorescence,[47] with the intensity proportional to the T_1 population. The scheme of the described $S_2(0^0) \leftarrow T_1(v) \leftarrow S_0(0_0)$ optical-optical double resonance (OODR) experiment[48-54] is shown in Figure 2a. Due to the lack of a_2 vibrational modes (Figure 2b), the excited state S_2 is symmetry-isolated from $S_2(^1A_1) \rightarrow S_1(^1A_2)$ spin-allowed nonradiative relaxation path. The alternative spin-forbidden paths, $S_2(^1A_1) \rightarrow T_2(^3A_1)$ and $S_2(^1A_1) \rightarrow T_1(^3A_2)$, are also inefficient because S_2 state is well-separated from the T_1 and T_2

states. The S_2/T_1 and S_2/T_2 crossing points have relatively high energies approaching the C-S dissociation limit and are not accessible at the ground vibrational level of S_2.[41] In addition, $S_2(^1A_1) \rightarrow T_1(^3A_2)$ path is also hindered by weak SOC between $^1A_1(\pi\pi^*)$ and $^3A_1(\pi\pi^*)$ states, as expected from the El-Sayed rule.[55]

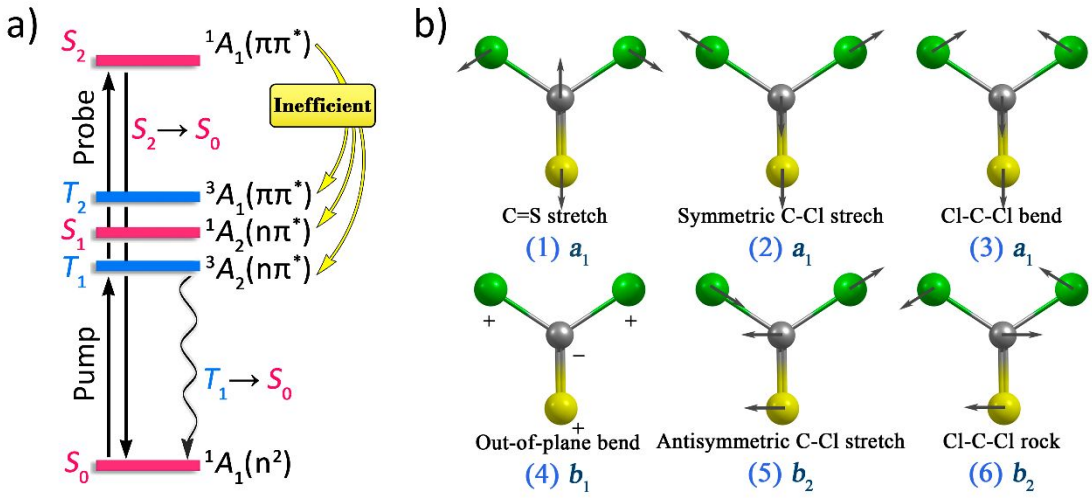

Figure 2. (a) Scheme of the OODR $S_2(0^0) \leftarrow T_1(v) \leftarrow S_0(0_0)$ experiment used to determine the $T_1(v)$ lifetime. The straight black arrows show absorption and emission, the yellow arrows show inefficient transitions from S_2 state, and the wavy black arrow indicates the $T_1 \rightarrow S_0$ ISC. (b) Normal vibrational modes of Cl_2CS. The numbers in parenthesis are the labels of vibrational modes.

The OODR technique was used by Fujiwara *et al*. to measure the T_1 lifetime in jet-cooled Cl_2CS at the rotational temperature of 1.5 K.[50] Using the nanosecond laser pulses, it was shown that the decay of T_1 state is biexponential with the short-lived component of ~20 ns attributed to the $T_1 \rightarrow S_0$ ISC and the long-lived component of ~4 μs caused by the weak T_1 phosphorescence.[50] Later, the six lowest T_1 vibrational states (0^0, 3^1, 4^2, 2^1, 3^2, and 4^4) lying within 600 cm^{-1} of the T_1 ZPE level were prepared using short picosecond pulses, and the individual short-lived components of these states were measured.[47] Surprisingly, the T_1 lifetime of ~20 ns disagrees with the previous

theoretical estimates of 0.02 ns[56] and 0.04 ns[57] predicted by the simple Fermi's golden rule. In this paper, we use our recent implementation of NA-TST combined with the Zhu-Nakamura transition probability to calculate the $T_1 \rightarrow S_0$ rate constants for the lowest T_1 vibrational states and provide insight into the nature of this ISC in thiophosgene.

2. Computational methods

The equilibrium geometries of the S_0 and T_1 states were found using the state-specific complete active space second-order perturbation theory (CASPT2)[58] and the coupled-cluster method with single, double, and perturbative triple excitations (CCSD(T))[59] as implemented in the Molpro[60] suite of programs. The stationary points on the T_1/S_0 crossing seam were located using an external script[61] modified to take advantage of the CCSD(T) numerical and CASPT2 analytical[62] gradients. The rate constants were calculated at the CASPT2/def2-TZVP[63] level of theory with (10,9) and (24,16) active spaces. The reduced mass, vibrational frequencies and moments of inertia for the minimum and turning point of the ground vibrational state were obtained with (10,9) active space. In addition to the MECP, we found a transition state crossing point (TSCP), which is a stationary point on the T_1/S_0 crossing seam surface characterized by a single imaginary frequency in the effective Hessian. The located S_0 and T_1 minima were proven to have no imaginary frequencies using the conventional vibrational analysis of the state-specific Hessian. In the cases of MECP and TSCP, the effective Hessian for the sloped intersection[27] was calculated as

$$\mathbf{H}_{\text{eff}} = \frac{\left|\mathbf{G}_1\right|\mathbf{H}_2 - \left|\mathbf{G}_2\right|\mathbf{H}_1}{\left|\mathbf{G}_1 - \mathbf{G}_2\right|}, \qquad (1)$$

where $\mathbf{G}_1$, $\mathbf{G}_2$ and $\mathbf{H}_1$, $\mathbf{H}_2$ are the gradients and the Hessian matrices of the S_0 and T_1 states, respectively. To obtain vibrational frequencies at the MECP (TSCP), one vibrational (aligned with the reaction coordinate), three translational, and three rotational degrees of freedom were projected out from the mass-weighted effective Hessian, $\mathbf{H}_{\text{eff}}^{\text{mw}}$ as follows

$$\mathbf{H}_{\text{proj}} = (\mathbf{I} - \mathbf{P})\mathbf{H}_{\text{eff}}^{\text{mw}}(\mathbf{I} - \mathbf{P}), \tag{2}$$

$$\mathbf{P} = \mathbf{P}_{\text{RC}} + \mathbf{P}_{\text{Tr}} + \mathbf{P}_{\text{Rot}}, \tag{3}$$

where $\mathbf{I}$ is the identity matrix and $\mathbf{P}$ is the projection matrix written as the sum of reaction coordinate, translational, and rotational projectors. The elements of the projection matrix[64] were found as

$$p_{3i-3+\gamma,3i'-3+\gamma'} = g_{3i-3+\gamma}g_{3i'-3+\gamma'} + \frac{\sqrt{m_i m_{i'}}}{M}\delta_{\gamma,\gamma'} + \sum_{\alpha,\beta}\sum_{\alpha',\beta'}\varepsilon_{\alpha\beta\gamma}a_{i\beta}Y_{\alpha,\alpha'}a_{i'\beta'}\varepsilon_{\alpha'\beta'\gamma'}. \tag{4}$$

Here i is the atomic index, indices α, β, γ referring to the x, y, z coordinates take values 1, 2 and 3, and g_k are the elements of the normalized difference gradient. This gradient is orthogonal to the crossing seam and defined as the difference between the S_0 and T_1 gradients at the MECP (TSCP). The other terms in Eq. (4) include the atomic masses m_i, total mass of the molecule M, Kronecker delta function $\delta_{\gamma,\gamma'}$, mass-weighted coordinates defined with respect to the center of mass $a_{i\beta}$, elements of the inverse moment of inertia tensor $Y_{\alpha,\alpha'}$, and Levi-Civita symbol $\varepsilon_{\alpha\beta\gamma}$. A similar projection technique was used to obtain vibrational frequencies at the turning points along the $T_1 \rightarrow S_0$ ISC path, with the difference gradient replaced by the gradient of the T_1 state. The density of vibrational states was calculated from the harmonic frequencies using a direct counting algorithm with the bin size of 1 cm^{-1}.[65] In the case of T_1 minimum, harmonic vibrational levels of

the 4th out-of-plane vibrational mode were replaced with those obtained by Fujiwara et al. from the solution of the symmetric double-well potential, described by the Gaussian-shape barrier augmented with quadratic, quartic, and hexic terms.[50] The moments of inertia were used to calculate the rotational densities of states for the asymmetric top model

$$\rho_{rot}(E_{rot}) = \frac{4\sqrt{2E_{rot}}}{\mathsf{h}^3}\sqrt{I_A I_B I_C}\,, \tag{5}$$

where E_{rot} is the rotational energy and $I_A \le I_B \le I_C$ are the principal moments of inertia. The rovibrational density of states was obtained via convolution of rotational and vibrational densities

$$\rho(E) = \int_0^E \rho_{rot}(E-\varepsilon)\rho_{vib}(\varepsilon)d\varepsilon\ . \tag{6}$$

To determine the reduced mass for the motion along the reaction coordinate, the mass-weighted Hessian was projected on the matrix $\mathbf{P}_{\mathrm{RC}}$ whose elements are given by the first term in Eq. (4)

$$\mathbf{H}'_{\mathrm{proj}} = \mathbf{P}_{\mathrm{RC}}\mathbf{H}^{\mathrm{mw}}_{\mathrm{eff}}\mathbf{P}_{\mathrm{RC}}\,. \tag{7}$$

The $\mathbf{H}'_{\mathrm{proj}}$ eigenvector $\mathbf{k}_\perp$ associated with a single non-zero eigenvalue was transformed from the mass-weighted to Cartesian coordinates, and the reduced mass was calculated as

$$\mu_\perp = \frac{1}{\mathbf{k}_\perp^{\mathrm{T}}\mathbf{k}_\perp}\,. \tag{8}$$

The ISC minimum energy path was found following the quadratic steepest decent[66] from the MECP to the T_1 and S_0 minima. The geometries corresponding to the turning points were reoriented with respect to the T_1 minimum to eliminate the translational and rotational contributions to the reaction coordinate. Specifically, the difference between the geometries at the turning points and T_1 minimum was minimized using the Nelder-Mead simplex algorithm with six

variables, namely three translational shifts and three orthogonal rotations.[67] The one-dimensional reaction coordinate r was calculated as the arc length along the reaction path

$$dr = \left(\sum_{i=1}^{3N} (dx_i)^2 \right)^{1/2}, \tag{9}$$

where dx is the difference between the Cartesian coordinates of the neighboring turning points. Once r was calculated, the triplet and singlet branches of the ISC path at the energies higher than the T_1 minimum were fit to quartic polynomials (see Supporting Information). Finally, the turning points along the reaction path were calculated with the energy step of 1 cm^{-1}.

The transition probability between T_1 and S_0 states, was found using the weak coupling (WC)[68] and Zhu-Nakamura (ZN)[69-73] formulas. The WC formula in terms of *spin-diabatic* parameters reads as

$$P_{trans}^{WC}(\varepsilon_\perp) = 4\pi^2 H_{SOC}^2 \left(\frac{2\mu_\perp}{\mathsf{h}^2 \bar{G} |\Delta \mathbf{G}|} \right)^{2/3} \mathrm{Ai}^2 \left(-(\varepsilon_\perp - E_{MECP}) \left(\frac{2\mu_\perp |\Delta \mathbf{G}|^2}{\mathsf{h}^2 \bar{G}^4} \right)^{1/3} \right). \tag{10}$$

Here $\hbar$ is the reduced Planck's constant, Ai(x) is the Airy function, $\varepsilon_\perp$ is the internal energy accumulated in the reaction coordinate, E_{MECP} is the barrier height given by the relative energy of the MECP, H_{SOC} is the spin-orbit coupling constant (SOC), $\mu_\perp$ is the reduced mass of the mode orthogonal to the crossing seam. The gradients of two PESs at the MECP ($\mathbf{G}_1$ and $\mathbf{G}_2$) appear in Eq. (10) in terms of $\bar{G} = (|\mathbf{G}_1 \mathbf{G}_2|)^{1/2}$ and $\Delta\mathbf{G}=\mathbf{G}_1-\mathbf{G}_2$. In contrast to the WC formula, the ZN probability is defined using *spin-adiabatic* parameters obtained after diagonalizing the *spin-diabatic* Hamiltonian along the ISC reaction coordinate

$$H = \begin{pmatrix} E_S & H_{SOC} \\ H_{SOC} & E_T \end{pmatrix}, \tag{11}$$

where diagonal elements are the energies of S_0 and T_1 states (Figure 3), and the off-diagonal term is the SOC constant calculated as a root mean square of the spin-orbit coupling matrix elements between all M_S components of the two electronic states.[27] These matrix elements were evaluated using the complete active space configuration interaction (CASCI) method[74] with the full-valence active space and the two-electron Breit-Pauli spin-orbit Hamiltonian.[2]

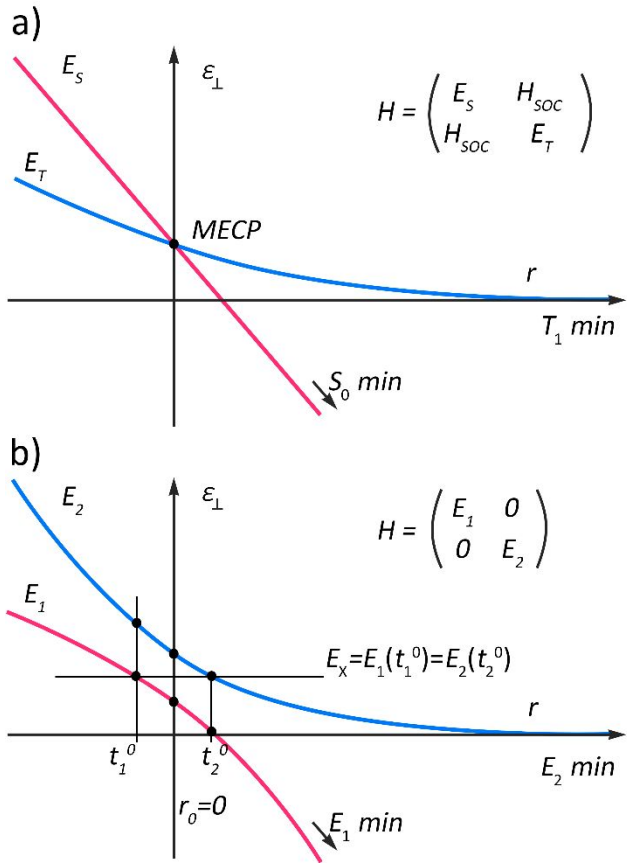

Figure 3. Intersection of S_0 and T_1 states along the reaction path r in the spin-diabatic (a) and spin-adiabatic (b) representations. The vertical axis coincides with the MECP geometry at r_0=0. The energy values defined by the black circles are used to calculate the parameters a and b.

Diagonalization of the spin-diabatic Hamiltonian (11) yields the spin-adiabatic states E_1 and E_2. The spin-adiabatic parameters for the sloped intersection a and $b(\varepsilon_\perp)$ were calculated as

$$a = \left[(d^2 - 1)^{1/2} \frac{\mathsf{h}^2}{\mu (t_2^0 - t_1^0)^2 \left(E_2(r_0) - E_1(r_0) \right)} \right]^{1/2}, \tag{12}$$

$$b(\varepsilon_\perp) = \left[(d^2 - 1)^{1/2} \frac{\varepsilon_\perp - \left(E_2(r_0) + E_1(r_0) \right)/2}{\left(E_2(r_0) - E_1(r_0) \right)/2} \right]^{1/2}, \tag{13}$$

$$d^2 = \frac{\left(E_2(t_1^0) - E_1(t_1^0) \right)\left(E_2(t_2^0) - E_1(t_2^0) \right)}{\left(E_2(r_0) - E_1(r_0) \right)^2}, \tag{14}$$

where t_1^0 and t_2^0 are the turning points at the E_{MECP}, as schematically shown in Figure 3; and r_0 is the point on the reaction path characterized by the smallest energy gap between the two spin-adiabatic potentials E_1 and E_2:

$$E_{MECP} = E_X = E_1(t_1^0) = E_2(t_2^0) = \frac{E_1(r_0) + E_2(r_0)}{2}. \tag{15}$$

The double passage ZN transition probability was calculated as

$$P_{trans}^{ZN}(\varepsilon_\perp) = 4 p_{ZN} (1 - p_{ZN}) \sin^2(\psi), \tag{16}$$

where p_{ZN} is the single passage transition probability, and ψ is the total phase describing the interference between the first and the second passages. Both p_{ZN} and ψ are piecewise defined with respect to E_X (b=0),

$$p_{ZN} = \begin{cases} \exp\left[-\dfrac{\pi}{4a} \sqrt{\dfrac{2}{b^2 + \sqrt{b^4 + 0.4a^2 + 0.7}}} \right], & b(\varepsilon_\perp) \geq 0 \\ \left[1 + B(\sigma/\pi) \exp(2\delta) - g_2 \sin^2(\sigma) \right]^{-1}, & b(\varepsilon_\perp) < 0 \end{cases} \tag{17}$$

$$\psi = \begin{cases} \sigma + \phi_S, \, b(\varepsilon_\perp) \geq 0 \\ arg(U_1), \, b(\varepsilon_\perp) < 0 \end{cases} . \quad (18)$$

The function $B(x)$, parameter g_2, Stokes constant U_1, and phases σ, δ, and ϕ_S are given in the ESI.

3. Results and discussion

According to the ergodicity assumption, the NA-TST rate constant is independent of time. As a result, the ISC rate obeys the first-order kinetic equation that is manifested in the exponential rate profile. The lifetime of the excited state is estimated as the inverse of the rate constant. The NA-TST can readily be applied to study kinetics of the $T_1 \rightarrow S_0$ ISC because of two reasons. First, the lifetime of T_1 excited state in Cl_2CS (20 ns) is long enough to expect the fast intramolecular vibrational energy redistribution. Second, there is an ISC barrier that has to be overcome to populate the ground S_0 state. Here, we consider only the nonradiative decay of T_1 neglecting phosphorescence because it is two orders of magnitude slower than the $T_1 \rightarrow S_0$ ISC.

The selected properties of Cl_2CS are summarized in Table 1, and the structural parameters are shown in Figure 4. The 0-0 gap between S_0 and T_1 states of 207.2 kJ mol^{-1} predicted at the CCSD(T)/def2-TZVP level of theory matches well the experimental value[50] of 209.3 kJ mol^{-1}. The gap increases by only 1.2 kJ mol^{-1}, if the larger def2-QZVP basis set is used. The calculated angles and bond lengths are in good agreement with those obtained from the microwave[75] and electron diffraction[76] experiments. However, the accuracy of the $T_1 \rightarrow S_0$ MECP barrier predicted by CCSD(T) is questionable as the T_1 and D_1 diagnostics indicate a significant multiconfigurational character of the S_0 state at the MECP (see ESI). A more accurate ISC barrier can be expected from the CASPT2 calculations as they better account for the multiconfigurational character of MECP.

The CASPT2(24,16) equilibrium geometries and vibrational frequencies are in good agreement with the experimental values (see ESI). Therefore, for predicting the ISC rate constants, we mostly rely on the predictions made with multireference CASPT2(24,16) method.

Table 1. Vertical, adiabatic and 0-0 excitation energies (kJ mol^{-1}) between S_0 and T_1 states. The energy barriers E_{MECP} and E_{TSCP} are reported with respect to the T_1 minimum. SOC values (cm^{-1}) are calculated with CASPT2(24,16) and corresponding basis set.

	CCSD(T)/ def2-TZVP	CCSD(T)/ def2-QZVP	CASPT2(10,9)/ def2-TZVP	CASPT2(24,16)/ def2-TZVP
ΔE_{vert}	241.7	242.0	223.0	226.4
ΔE_{adiab}	209.2	210.3	191.6	194.5
[a]$\Delta E_{0\text{-}0}$	206.0	207.2	188.7	191.5[a]
E_{MECP}	46.1	46.7	38.1	35.0
E_{TSCP}	74.0	75.8	66.9	63.8
SOC at MECP	141	134	155	157
SOC at TSCP	186	181	187	187

[a] Estimated from the T_1 and S_0 ZPEs obtained with CASPT2(10,9)/def2-TZVP

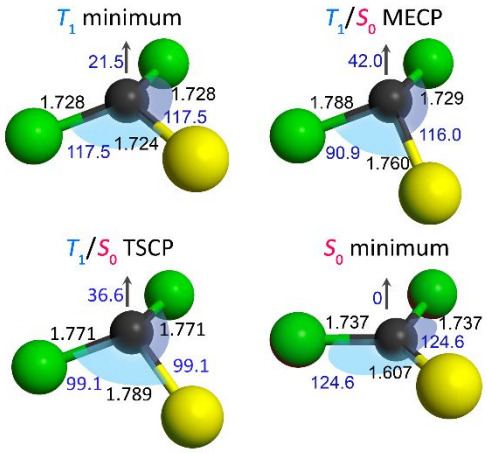

Figure 4. Minima and crossing points (MECP and TSCP) on the T_1 and S_0 PESs. Bond lengths (black, Å) and angles (blue, degrees) are calculated at the CASPT2(24,16)/def2-TZVP level of theory.

While the ground state of Cl_2CS is planar (C_{2v} symmetry), the T_1 excited state has a pyramidal (C_s symmetry) configuration as illustrated in Figure 4. The MECP geometry was also expected to have C_s symmetry, however we could not locate such a structure using the linear interpolation between the T_1 and S_0 minima as the initial guess. Instead, we searched for the MECP distorting the T_1 geometry along the normal vibrational modes. This search produced two stationary points on the T_1/S_0 crossing seam: one is the true MECP and another one is the transition state crossing point (TSCP). The latter is a saddle point on the crossing seam characterized by a single imaginary frequency in the effective Hessian. This frequency corresponds to the vibrational motion that connects two equivalent MECPs being the mirror images of each other. The MECP barrier found with CASPT2(24,16) is only 35.0 kJ mol^{-1} with respect to the T_1 minimum, while the TSCP barrier is 63.8 kJ mol^{-1}.

The T_1→MECP path is not aligned with any of the vibrational modes but rather appears as a linear combination of several vibrations with a significant contribution from the out-of-plane distortion, Cl−C−S bending, and C−S stretching. The T_1 pyramidal configuration undergoes the out-of-plane angle expansion from 21.5° to 42.0° at the MECP, which is followed by the angle contraction until the planar geometry of the S_0 state is reached. On the other hand, either one of the two Cl−C−S angles decreases from 117.5° to 90.9° and then expands from 90.9° to 124.6° along the T_1→MECP→S_0 path. Thus, two chiral MECP structures can be attained depending on which of the two Cl−C−S angles is changing along the reaction coordinates. Since the symmetry numbers of the MECP (C_1) and T_1 minimum (C_s) are both equal to one, and there are two equivalent MECPs, the overall T_1→S_0 ISC path is doubly degenerate. In the case of the backward S_0→T_1 ISC, the degeneracy of the path increases to four because of the symmetry number of S_0

minimum (C_{2v}) is equal to two. However, the effect of backward $S_0 \rightarrow T_1$ ISC on the T_1 decay is expected to be negligible because of the large energy gap between the S_0 minimum and MECP. The C−S bond is elongated both in the T_1 minimum (1.724 Å) and the MECP (1.760 Å), compared with the S_1 minimum (1.607 Å). This elongation is caused by population of the π^*(C−S) orbital that reduces the C−S bond order. The occupation numbers of the selected natural orbitals at the critical points on the singlet and triplet PESs are shown in Figure 5. While the occupation numbers of the S_0 state π(C−S) and π^*(C−S) orbitals are close to 2 and 0 at the S_0 minimum, they become equal to 1.749 and 0.263 at MECP. These occupation numbers together with the coupled-cluster diagnostics (T_1=0.039 and D_1=0.181) indicate a multiconfigurational character of the S_0 state at the MECP. In contrast, the T_1 state has no significant multiconfigurational character at the three critical points (T_1 minimum, TSCP and MECP) relevant to the ISC rate calculations.

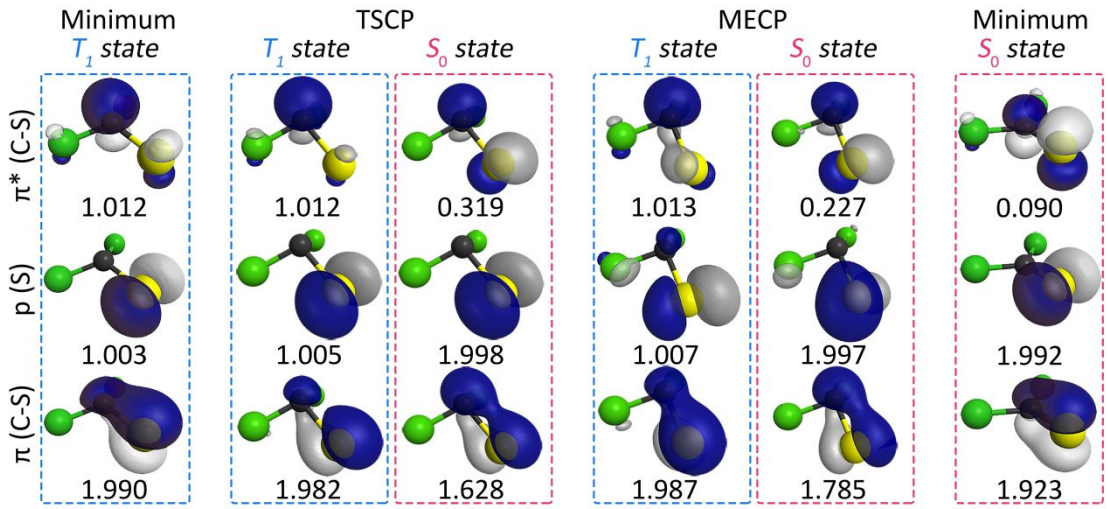

Figure 5. Selected CASSCF natural orbitals and their occupation numbers for the T_1 minimum, MECP, TSCP, and S_0 minimum. The calculations performed at the CASPT2(24,16)/def2-TZVP level of theory.

Overall, the $T_1 \rightarrow S_0$ ISC path is reminiscent to the breathing motion, which suggests a sloped PES intersection at the MECP (Figure 6, upper panel). Indeed, the collinear S_0 and T_1 energy gradients point to the same direction at the MECP. The SOC between the T_1 and S_0 states at the MECP is relatively weak and equals to 157 cm^{-1}. However, the SOC at the turning points along the reaction path is 189 cm^{-1} and does not change significantly in the energy range of interest limited by 600 cm^{-1} above the T_1 ZPE level (Figure 6, lower panel).

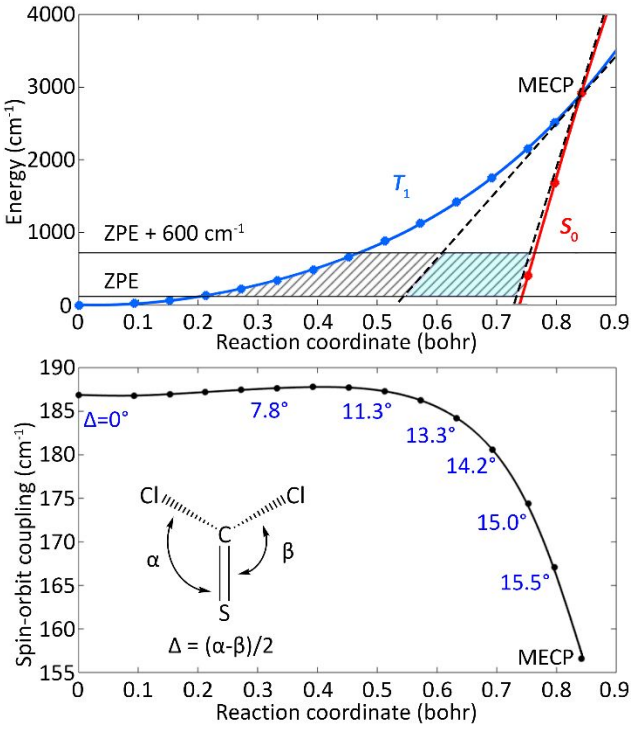

Figure 6. Upper panel: The $T_1 \rightarrow S_0$ ISC path through the MECP. Solid blue and red curves are the quartic polynomials fitted to the turning points on the calculated steepest descent paths starting at the MECP. The black dashed lines are simple linear potentials with the slopes defined by the energy gradients at the MECP. The shaded area shows the barrier widths in the region of interest (600 cm^{-1} above the T_1 ZPE) for the models with quartic potential (ZN transition probability) and linear potential (WC transition probability). Lower panel: The spin-orbit coupling variation along the reaction coordinate.

The vibrational levels of the T_1 state populated in the OODR experiment lie well below the MECP and, therefore, the $T_1 \rightarrow S_0$ ISC takes place in the quantum tunneling regime. To calculate the ISC rate constants for different T_1 vibrational states, the density of rovibrational states at the turning points along the reaction path have to determined.[26] In microcanonical transition state theory, these densities are usually replaced with the density calculated at the transition state.[77, 78] In the NA-TST, it is also tempting to rely on the rovibrational density of states at the MECP. However, this approximation is expected to be poor in the case of Cl_2CS because the turning points of interest are far away from the MECP. Instead, we obtain the rovibrational density of states from the lowest turning point accessible by the molecules with vibrational energy equal to ZPE. This turning point of the ground vibrational state can be found iteratively, solving the following equation for r

$$\varepsilon_{\perp}(r) = \frac{1}{2}\sum_{i=1}^{3N-6} \mathsf{h}\omega_i - \frac{1}{2}\sum_{i=1}^{3N-7} \mathsf{h}\omega_i'(r), \tag{19}$$

where r is the arc length along the reaction coordiante ($r = 0$ at the T_1 minimum), $\varepsilon_{\perp}(r)$ is the relative energy of the turning point with respect to the T_1 minimum, ω_i and ω_i' are the harmonic vibrational frequencies at the T_1 minimum and turning point, respectively. The first sum in Eq. (19) is the T_1 ZPE and the second sum, which excludes reaction coordinate, is the ZPE at the turning point for a given r. Using CASPT2(10.9)/def2-TZVP and setting the energy threshold to 5 cm^{-1}, we found that the turning point of the ground vibrational state lies 124 cm^{-1} above the T_1 minimum. This value is much smaller than the ZPE difference between the T_1 minimum and MECP that is equal to 283 cm^{-1}. Taking ΔZPE as the difference between the ZPEs of T_1 minimum and the turning point, the microcanonical rate constant for the tunneling regime can be written as

$$k(E) = \frac{1}{h\rho_R} \int_{\Delta ZPE}^{E+\Delta ZPE} \rho_{TP}^{0}(E + \Delta ZPE - \varepsilon_\perp) P_{trans}(\varepsilon_\perp) d\varepsilon_\perp \,, \tag{20}$$

where E is the total internal energy, h is the Planck constant, ρ_R is the reactant density of rovibrational states, ρ_{TP}^{0} is the density of rovibrational states at the turning point corresponding to the ground vibrational state, $\varepsilon_\perp$ is the energy accumulated in the reaction coordinate, and $E - \varepsilon_\perp$ is the energy partitioned into spectator degrees of freedom. The ZPE correction scheme (ZPE1) defined by Eq. (20) is equivalent to lowering the MECP barrier by ΔZPE. The $T_1 \rightarrow S_0$ ISC rate constants calculated using Eq. (20) combined with Eqs. (10) and (16) are reported in Figure 7 and Table 2.

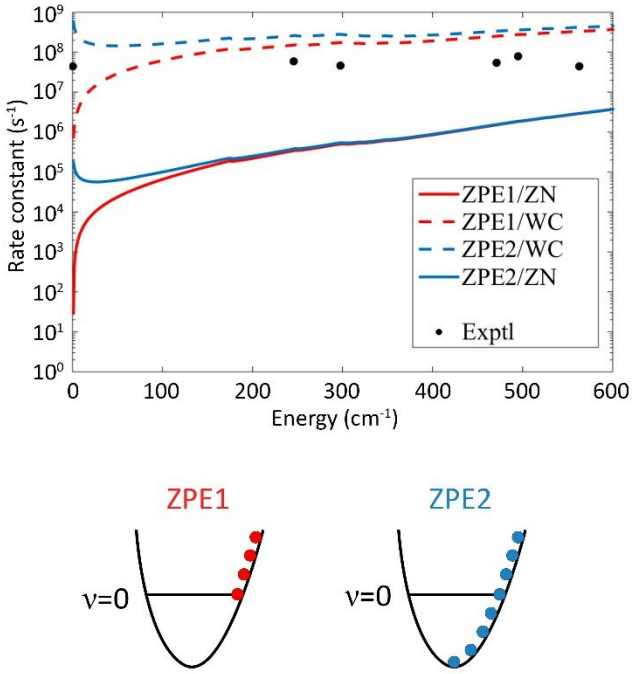

Figure 7. Upper panel: The $T_1 \rightarrow S_0$ ISC rate constant calculated using the WC (dashed) and ZN (solid) transition probabilities at the CASPT2/def2-TZVP level of theory. Red and blue curves

indicate the ZPE1 and ZPE2 correction schemes, respectively. Lower panel: The turning points contributing to the rate constant in the ZPE1 and ZPE2 schemes.

Table 2. The $T_1 \rightarrow S_0$ ISC rate constants (s^{-1}) calculated at the CASPT2/def2-TZVP level of theory. The experimental rate constants are obtained as the inverse of the reported T_1 lifetimes.

Energy level, cm^{-1}		Active space (10,9)				Active space (24,16)		exptl.[47]
		ZPE1		ZPE2		ZPE2		
		WC	ZN	WC	ZN	WC	ZN	
$T_1(0^0)$	0	1.1×10^6	2.7×10^1	7.7×10^8	1.6×10^5	2.3×10^9	3.1×10^5	4.4×10^7
$T_1(3^1)$	246	2.1×10^8	3.2×10^5	3.5×10^8	3.5×10^5	1.0×10^9	8.5×10^5	5.9×10^7
$T_1(4^2)$	298	2.4×10^8	4.8×10^5	3.8×10^8	5.1×10^5	1.1×10^9	1.3×10^6	4.6×10^7
$T_1(2^1)$	471	3.9×10^8	1.6×10^6	5.1×10^8	1.7×10^6	1.5×10^9	4.4×10^6	5.4×10^7
$T_1(3^2)$	495	4.1×10^8	1.9×10^6	5.4×10^8	1.9×10^6	1.6×10^9	5.2×10^6	8.0×10^7
$T_1(4^4)$	563	4.8×10^8	2.9×10^6	6.0×10^8	3.0×10^6	1.7×10^9	8.1×10^6	4.4×10^7

Let us first discuss the CASPT2(10,9) rate constants for all vibrational states except $T_1(0^0)$. The ZPE1/WC rate constants are almost an order of magnitude greater than the experimental values, while the ZPE1/ZN rate constants are about two orders of magnitude smaller. These results can be rationalized by looking at the width of the MECP barrier. The WC formula does not account for the curvature of the crossing PESs, assuming that they cross linearly with the slopes given by the energy gradients at the MECP. As shown in Figure 6, the barrier width used to calculate the WC transitions probability (highlighted) is only about 0.15 bohr, while the actual width of the MECP barrier varies from 0.5 to 0.2 bohr in the region of interest. In contrast to the WC transition probability expression, the ZN formula accounts for the curvature of crossing PESs through the imaginary action integrals and provides a correct treatment of the barrier width. Thus, a good agreement between the ZPE1/WC rate constants and the experimental measurements is entirely accidental and can be attributed to the drastically underestimated barrier width. It is interesting to note that the ZPE1/ZN rate constants approach experimental rates at the high energies; the calculated rate constant for the $T_1(4^4)$ state is k=2.9×10^6 s^{-1} (τ=345 ns), while the experimental

value is k=4.4×10^7 s^{-1} (τ=23 ns). However, there is a very large deviation at the energies below 100 cm^{-1}. The OODR experiment shows that $T_1(0^0)$ decays as fast as the other vibrational states, while the ZPE1/ZN predicts the dramatic reduction of the ISC rate by six orders of magnitude. We believe that this discrepancy arises from neglecting the tunneling contribution from the reaction path segment located below the ZPE1 turning point, where the decrease of potential energy is compensated by the increase in kinetic energy. To account for this segment of the reaction path, the lower integration limit in Eq. (20) must be set to zero,

$$k(E) = \frac{1}{h\rho_R} \int_0^{E+\Delta ZPE} \rho_{TP}^0(E + \Delta ZPE - \varepsilon_\perp) P_{trans}(\varepsilon_\perp) d\varepsilon_\perp \ . \qquad (21)$$

The resulting ZPE2 correction scheme greatly improves the rate constants below 100 cm^{-1}, while predicting the values similar to the ZPE1 scheme at higher energy. The expansion of the active space from (10,9) to (24,16) results in lowering the MECP barrier and producing the rate constants that are closer to the experimental values. At the CASPT2(24,16)/def2-TZVP level of theory, the predicted and experimental lifetimes for $T_1(0^0)$ are 123 and 23 ns, respectively. We believe that the overestimated lifetime can be explained by the tunneling taking place away from the minimum energy reaction path going through MECP, where the barrier is narrower and the tunneling is more efficient. To account for the effect of multidimensional tunneling a further development of NA-TST is required. One of the promising directions would be to sample multiple ISC reaction paths crossing the seam surface between MECPs and TSCPs.

4. Conclusions

We demonstrated that the $T_1 \rightarrow S_0$ ISC in thiophosgene is driven by quantum tunneling through the barrier formed by the crossing T_1 and S_0 electronic states. The minimum energy crossing point between these two states was located with the single-reference CCSD(T) and multireference CASPT2 electronic structure methods. Using the nonadiabatic transition state theory with the weak coupling and Zhu-Nakamura transition probabilities, we calculated the $T_1 \rightarrow S_0$ rate constants and estimated the lifetimes of the lowest T_1 vibrational states.

A good agreement between the experimental rate constants and those predicted by NA-TST with the WC probability of transition formula appears to be accidental and can be explained by the heavily underestimated width of the ISC barrier. Therefore, at the crossing regions were two potentials deviate significantly from the linear model, the traditional WC probability formula must be used with caution. In such cases, one can resort to either the improved form of the WC formula that has recently been suggested,[34] or to the Zhu-Nakamura transition probability expressions. The latter not only accounts for the curvature of the crossing potentials but also expands the NA-TST applications to the situations with relatively strong spin-orbit coupling.

The $T_1 \rightarrow S_0$ ISC rate constants obtained with the NA-TST/ZN and CASPT2(24,16)/def-TZVP level of theory are from one to two orders of magnitude smaller than the rates obtained from the experimental T_1 lifetimes. Although the errors in the barrier and ZPEs predicted by CASPT2 should not be dismissed, we believe that the main deviation is due to the multidimensional tunneling that is not accounted for in the simple one-dimensional statistical theories such as NA-TST. One way to improve these results is to search for the alternative ISC

tunneling paths with the narrower barriers, similar to the approaches developed for the conventional single-state transition state theory.[79] We also proposed a new ZPE correction scheme that account for the tunneling at low potential energies and significantly improves the prediction for microcanonical rate constants at low internal energies. This new ZPE scheme explains why the $T_1(0^0)$ state of thiophosgene decays at the rate comparable to the other vibrational states.

Notes

Electronic supplementary information (ESI) available: (a) Atomic and internal coordinates of the minima and crossing points. (b) Natural bonding orbitals of (24,16) active space and their occupation numbers. (c) Details on the Zhu-Nakamura formulas.

Conflicts of interest

There are no conflicts to declare.

Acknowledgements

This work was supported by the National Science Foundation through a CAREER Award (CHE-1654547) to S.A.V.

References

1. C. M. Marian, *Wiley Interdisciplinary Reviews: Computational Molecular Science*, 2012, **2**, 187-203.

2. D. G. Fedorov, S. Koseki, M. W. Schmidt and M. S. Gordon, *International Reviews in Physical Chemistry*, 2003, **22**, 551-592.

3. N. Matsunaga and S. Koseki, in *Reviews in Computational Chemistry*2004, vol. 20, pp. 101-152.

4. B. Soep, J. M. Mestdagh, M. Briant, M. A. Gaveau and L. Poisson, *Phys Chem Chem Phys*, 2016, **18**, 22914-22920.

5. A. Rodriguez-Serrano, V. Rai-Constapel, M. C. Daza, M. Doerr and C. M. Marian, *Phys Chem Chem Phys*, 2015, **17**, 11350-11358.

6. W. Zhang and K. J. Gaffney, *Acc Chem Res*, 2015, **48**, 1140-1148.

7. O. Yushchenko, G. Licari, S. Mosquera-Vazquez, N. Sakai, S. Matile and E. Vauthey, *J Phys Chem Lett*, 2015, **6**, 2096-2100.

8. S. K. Lower and M. A. El-Sayed, *Chemical Reviews*, 1966, **66**, 199-241.

9. L. Martínez-Fernández, I. Corral, G. Granucci and M. Persico, *Chemical Science*, 2014, **5**, 1336.

10. S. J. Klippenstein, *Proceedings of the Combustion Institute*, 2017, **36**, 77-111.

11. X. Li, A. W. Jasper, J. Zádor, J. A. Miller and S. J. Klippenstein, *Proceedings of the Combustion Institute*, 2017, **36**, 219-227.

12. L. A. Fredin, M. Papai, E. Rozsalyi, G. Vanko, K. Warnmark, V. Sundstrom and P. Persson, *J Phys Chem Lett*, 2014, **5**, 2066-2071.

13. Y. Liu, P. Persson, V. Sundstrom and K. Warnmark, *Acc Chem Res*, 2016, **49**, 1477-1485.

14. P. Zimmer, L. Burkhardt, A. Friedrich, J. Steube, A. Neuba, R. Schepper, P. Muller, U. Florke, M. Huber, S. Lochbrunner and M. Bauer, *Inorg Chem*, 2018, **57**, 360-373.

15. W. Fan, P. Huang and X. Chen, *Chem Soc Rev*, 2016, **45**, 6488-6519.

16. G. Obaid, M. Broekgaarden, A. L. Bulin, H. C. Huang, J. Kuriakose, J. Liu and T. Hasan, *Nanoscale*, 2016, **8**, 12471-12503.

17. J. Zhao, W. Wu, J. Sun and S. Guo, *Chem Soc Rev*, 2013, **42**, 5323-5351.

18. L. A. Baker, S. L. Clark, S. Habershon and V. G. Stavros, *J Phys Chem Lett*, 2017, **8**, 2113-2118.

19. K. Yamazaki, Y. Miyazaki, Y. Harabuchi, T. Taketsugu, S. Maeda, Y. Inokuchi, S. N. Kinoshita, M. Sumida, Y. Onitsuka, H. Kohguchi, M. Ehara and T. Ebata, *J Phys Chem Lett*, 2016, **7**, 4001-4007.

20. B. S. Gerstman and N. Sungar, *The Journal of Chemical Physics*, 1992, **96**, 387-398.

21. Y. Kitagawa, Y. Chen, N. Nakatani, A. Nakayama and J. Hasegawa, *Phys Chem Chem Phys*, 2016, **18**, 18137-18144.

22. D. A. Fedorov, S. R. Pruitt, K. Keipert, M. S. Gordon and S. A. Varganov, *J Phys Chem A*, 2016, **120**, 2911-2919.

23. Q. Cui, K. Morokuma, J. M. Bowman and S. J. Klippenstein, *The Journal of Chemical Physics*, 1999, **110**, 9469.

24. J. N. Harvey, S. Grimme, M. Woeller, S. D. Peyerimhoff, D. Danovich and S. Shaik, *Chemical Physics Letters*, 2000, **322**, 358-362.

25. J. N. Harvey and M. Aschi, *Physical Chemistry Chemical Physics*, 1999, **1**, 5555-5563.

26. J. C. Lorquet and B. Leyh-Nihant, *The Journal of Physical Chemistry*, 1988, **92**, 4778-4783.

27. A. O. Lykhin, D. S. Kaliakin, G. E. DePolo, A. A. Kuzubov and S. A. Varganov, *International Journal of Quantum Chemistry*, 2016, **116**, 750-761.

28. A. Farazdel and M. Dupuis, *Journal of Computational Chemistry*, 1991, **12**, 276-282.

29. T. Chachiyo and J. H. Rodriguez, *J Chem Phys*, 2005, **123**, 94711.

30. N. Koga and K. Morokuma, *Chemical Physics Letters*, 1985, **119**, 371-374.

31. D. S. Kaliakin, D. G. Fedorov, Y. Alexeev and S. A. Varganov, *J Chem Theory Comput*, 2019, **15**, 6074-6084.

32. E. E. Nikitin and S. Y. Umanskii, *Theory of slow atomic collisions*, Springer, Berlin, 1984.

33. E. E. Nikitin, *Annu Rev Phys Chem*, 1999, **50**, 1-21.

34. E. I. Dashevskaya, E. E. Nikitin and H.-J. Troe, *Zeitschrift für Physikalische Chemie*, 2018, **232**, 311-323.

35. Y. Fan, J. Chen, L. Yu, A. Li, G. Zhai, Y. Lei and C. Zhu, *Phys Chem Chem Phys*, 2018, **20**, 2260-2273.

36. T. Murakami, M. Nakazono, A. Kondorskiy, T. Ishida and S. Nanbu, *Phys Chem Chem Phys*, 2012, **14**, 11546-11555.

37. H. Nakamura, *J Phys Chem A*, 2006, **110**, 10929-10946.

38. C. Xu, L. Yu, C. Zhu, J. Yu and Z. Cao, *Sci Rep*, 2016, **6**, 26768.

39. M. Yang, C. Huo, A. Li, Y. Lei, L. Yu and C. Zhu, *Phys Chem Chem Phys*, 2017, **19**, 12185-12198.

40. L. Zhao, P. W. Zhou, B. Li, A. H. Gao and K. L. Han, *J Chem Phys*, 2014, **141**, 235101.

41. L. Lin, F. Zhang, W. J. Ding, W. H. Fang and R. Z. Liu, *J Phys Chem A*, 2005, **109**, 554-561.

42. E. Berrios, P. Sundaradevan and M. Gruebele, *J Phys Chem A*, 2013, **117**, 7535-7541.

43. P. D. Chowdary and M. Gruebele, *J Chem Phys*, 2009, **130**, 024305.

44. T. S. Einfeld, C. Maul, K.-H. Gericke and A. Chichinin, *The Journal of Chemical Physics*, 2002, **117**, 1123-1129.

45. A. R. W. McKellar and B. E. Billinghurst, *Journal of Molecular Spectroscopy*, 2015, **315**, 24-29.

46. D. C. Moule, T. Fujiwara and E. C. Lim, in *Advances in Photochemistry*2005, pp. 27-79.

47. T. Fujiwara and E. C. Lim, *J Chem Phys*, 2008, **129**, 041102.

48. R. W. Field, *Faraday Discussions of the Chemical Society*, 1981, **71**, 111-123.

49. R. N. Dixon and C. M. Western, *Journal of Molecular Spectroscopy*, 1986, **115**, 74-81.

50. T. Fujiwara, E. C. Lim, R. H. Judge and D. C. Moule, *J Chem Phys*, 2006, **124**, 124301.

51. T. Fujiwara, E. C. Lim, J. Kodet, R. H. Judge and D. C. Moule, *Journal of Molecular Spectroscopy*, 2005, **232**, 331-340.

52. T. Fujiwara, E. C. Lim and D. C. Moule, *The Journal of Chemical Physics*, 2003, **119**, 7741-7748.

53. T. Fujiwara, D. C. Moule and E. C. Lim, *The Journal of Physical Chemistry A*, 2003, **107**, 10223-10227.

54. T. Fujiwara, D. C. Moule and E. C. Lim, *Chemical Physics Letters*, 2004, **389**, 165-170.

55. M. A. El-Sayed, *The Journal of Chemical Physics*, 1963, **38**, 2834-2838.

56. D. C. Moule, I. R. Burling, H. Liu and E. C. Lim, *The Journal of Chemical Physics*, 1999, **111**, 5027-5037.

57. S. Rashev, D. C. Moule and S. T. Djambova, *Chemical Physics Letters*, 2007, **441**, 43-47.

58. H. J. Werner, *Molecular Physics*, 1996, **89**, 645-661.

59. J. D. Watts, J. Gauss and R. J. Bartlett, *The Journal of Chemical Physics*, 1993, **98**, 8718-8733.

60. H.-J. Werner, P. J. Knowles, G. Knizia, F. R. Manby and M. Schütz, *Wiley Interdisciplinary Reviews: Computational Molecular Science*, 2012, **2**, 242-253.

61. J. N. Harvey, M. Aschi, H. Schwarz and W. Koch, *Theoretical Chemistry Accounts*, 1998, **99**, 95-99.

62. P. Celani and H. J. Werner, *The Journal of Chemical Physics*, 2003, **119**.

63. F. Weigend and R. Ahlrichs, *Physical Chemistry Chemical Physics*, 2005, **7**, 3297-3305.

64. W. H. Miller, N. C. Handy and J. E. Adams, *The Journal of Chemical Physics*, 1980, **72**, 99.

65. T. Baer and W. L. Hase, *Unimolecular Reaction Dynamics: Theory and Experiments*, Oxford University Press, New York, 1995.

66. J. Q. Sun, K. Ruedenberg and G. J. Atchity, *The Journal of Chemical Physics*, 1993, **99**, 5276-5280.

67. J. C. Lagarias, J. A. Reeds, M. H. Wright and P. E. Wright, *SIAM Journal on Optimization*, 1998, **9**, 112-147.

68. E. E. Nikitin, *Optics and Spectroscopy*, 1961, **11**, 246-248.

69. C. Zhu and H. Nakamura, *The Journal of Chemical Physics*, 1992, **97**, 8497-8514.

70. C. Zhu and H. Nakamura, *The Journal of Chemical Physics*, 1994, **101**, 10630-10647.

71. C. Zhu and H. Nakamura, *The Journal of Chemical Physics*, 1994, **101**, 4855-4866.

72. C. Zhu, H. Nakamura, N. Re and V. Aquilanti, *The Journal of Chemical Physics*, 1992, **97**, 1892-1904.

73. C. Y. Zhu, Y. Teranishi and H. Nakamura, *Adv Chem Phys*, 2001, **117**, 127-233.

74. B. H. Lengsfield, *The Journal of Chemical Physics*, 1981, **74**, 6849.

75. J. H. Carpenter, D. F. Rimmer, J. G. Smith and D. H. Whiffen, *J. Chem. Soc., Faraday Trans. 2,* , 1975, **71**, 1752-1762.

76. M. Nakata, T. Fukuyama and K. Kuchitsu, *Journal of Molecular Structure*, 1982, **81**, 121-129.

77. S. Kato and K. Morokuma, *The Journal of Chemical Physics*, 1980, **72**, 206-217.

78. W. H. Miller, *Journal of the American Chemical Society*, 1979, **101**, 6810-6814.

79. J. L. Bao and D. G. Truhlar, *Chem Soc Rev*, 2017, **46**, 7548-7596.